AGU PUBLICATIONS

JGR

Journal of Geophysical Research: Planets

RESEARCH ARTICLE
10.1002/2017JE005364

Key Points:
- The nonmare mafic interior of SPA is dominated by pyroxene-rich mineralogies
- Systematic, roughly concentric zones of pyroxene composition and abundance are recognized across the basin
- Although Mg-rich pyroxenes are pervasive across SPA, the innermost zone exhibits distinctive Ca,Fe-rich pyroxene

Supporting Information:
- Supporting Information S1

Correspondence to:
D. P. Moriarty III,
daniel.p.moriarty@nasa.gov

Citation:
Moriarty, D. P., III & Pieters, C. M. (2018). The character of South Pole-Aitken Basin: Patterns of surface and subsurface composition. *Journal of Geophysical Research: Planets*, *123*, 729–747. https://doi.org/10.1002/2017JE005364

Received 16 JUN 2017
Accepted 12 FEB 2018
Accepted article online 20 FEB 2018
Published online 11 MAR 2018

The Character of South Pole-Aitken Basin: Patterns of Surface and Subsurface Composition

D. P. Moriarty III[1] and **C. M. Pieters**[2]

[1]Planetary Geology, Geophysics, and Geochemistry Laboratory, NASA GSFC, Greenbelt, MD, USA, [2]Department of Earth, Environmental, and Planetary Sciences, Brown University, Providence, RI, USA

Abstract Using Moon Mineralogy Mapper data, we characterize surface diversity across the enormous South Pole-Aitken Basin (SPA) by evaluating the abundance and composition of pyroxenes, which are overwhelmingly the most abundant mafic mineral in the region. Although SPA exhibits significant complexity due to billions of years of geologic processes subsequent to formation, the basin has retained regular patterns of compositional heterogeneity across its structure. Four distinct, roughly concentric zones are defined: (1) a central SPA compositional anomaly, which exhibits a pervasive elevated Ca,Fe-rich pyroxene abundance; (2) a Mg-pyroxene annulus, which is dominated by abundant Mg-rich pyroxenes; (3) a heterogeneous annulus, which exhibits localized pyroxene-rich areas spatially mixed with feldspathic materials; and (4) the SPA exterior, which is primarily feldspathic. Pyroxene compositions in the heterogeneous annulus are similar to those in the Mg-pyroxene annulus, and Mg-rich pyroxenes also underlie the more Ca,Fe-rich pyroxene surface material across the SPA compositional anomaly. The establishment of these four distinct compositional zones across SPA constrains basin evolution models and serves to guide potential sample return (and other science) targets.

Plain Language Summary The South Pole-Aitken Basin is a vast impact structure on the far side of the Moon. In this study, we look at the compositional structure of the basin using data from orbital instruments. We find that this massive basin exhibits several distinct compositional zones. These zones arise from incredibly energetic processes associated with the impact event, which excavated and melted rocks from deep beneath the lunar surface. Later in lunar history, volcanic processes and additional impacts further shaped the basin interior. We identify an anomalous ~650 km region in central South Pole-Aitken, which exhibits an unusual composition, raising questions about its origin. These results have implications for our understanding of lunar evolution and the formation of large impact basins. Additionally, these results may help in the selection of landing sites for anticipated sample return and other science missions.

1. Introduction

As the largest definitive impact structure on the Moon (Garrick-Bethell & Zuber, 2009; Spudis et al., 1994; Stuart-Alexander, 1978), the South Pole-Aitken Basin (SPA) undoubtedly shaped the course of lunar history. Through analysis of existing remote sensing data and anticipated SPA samples (Jolliff et al., 2003, 2010, 2017), a number of fundamental and diverse lunar science questions can be addressed. Relevant issues include the composition of the lower crust and/or upper mantle, the absolute ages of lunar impact basins and other features, and the physical and compositional implications of the large-scale impacts that forged our solar system.

For stratified targets such as the primary lunar crust, basin formation models can be used to interpret the post-impact distribution of materials arising from processes such as excavation and impact melting (Cintala & Grieve, 1994; Hammond et al., 2009; Hurwitz & Kring, 2014; Melosh, 1989; Morrison, 1998; Potter et al., 2012; Stewart, 2011; Vaughan et al., 2013; Vaughan & Head, 2014). The observed spatial distribution of materials places constraints on the basin formation process, as well as the preimpact stratigraphy of the crust and upper mantle. Because SPA is the largest impact structure on the Moon, materials excavated by the SPA-forming impact may represent some of the deepest lunar materials available for study.

In this paper, we investigate the character and distribution of materials across SPA using relatively high spatial and spectral resolution data from the Moon Mineralogy Mapper (M^3). The detailed maps of pyroxene composition and abundance analyzed here trace mineralogical diversity across SPA, placing important constraints on basin formation models, and potentially guiding future sample return missions (such as MoonRise; Jolliff et al., 2003, 2010, 2017).

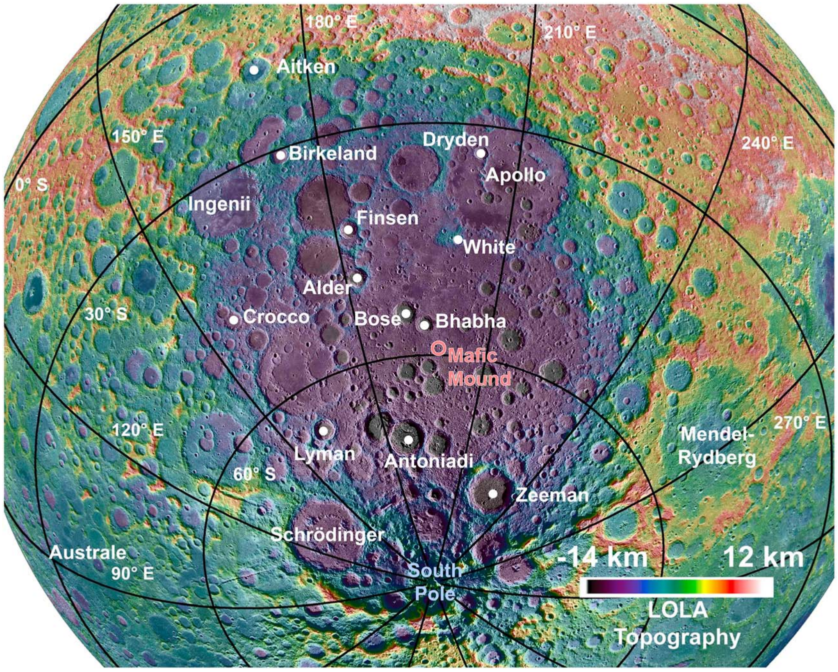

Figure 1. The topography of the South Pole-Aitken Basin as revealed by the Lunar Orbiter Laser Altimeter (LOLA) (Smith et al., 2010), superimposed over a Lunar Reconnaissance Orbiter Wide Angle Camera (WAC) (Robinson et al., 2010) mosaic. At approximately 2,500 km in diameter, SPA extends across a significant fraction of the far side of the Moon. The locations of several prominent craters are labeled with white dots at their centers. The names of several impact basins are written across their interiors. Mafic Mound is indicated with an open red circle. The South Pole is labeled in blue text.

2. Background

2.1. The Significance and Composition of SPA

As seen in Figure 1, the ~2,300 km SPA is one of the defining features of the Moon, covering a significant fraction of the lunar surface (e.g., Garrick-Bethell & Zuber, 2009). Given its large size, SPA may have had profound petrological and geophysical effects both regionally and globally. For instance, large lunar impacts have been implicated in (a) the production of melt seas that may cool slowly, convect, and differentiate (Cassanelli & Head, 2016; Hurwitz & Kring, 2014; Morrison, 1998; Vaughan & Head, 2014; Warren et al., 1996); (b) localized mantle convection (Elkins-Tanton & Hager, 2005); (c) antipodal and/or global magma ascent (Kring et al., 2015; Schultz & Crawford, 2011); or even (d) cumulate overturn of the mantle (e.g., Kring et al., 2015). In any scenario, basin-forming impacts are extremely energetic events that have the potential to influence the course of a planet's evolution.

In general, SPA materials are enriched in mafic minerals relative to the highlands feldspathic crust (e.g., Lawrence et al., 2002; Pieters et al., 2001). Across the basin, the most common nonmare mafic component appears to be Mg-rich, low-Ca pyroxenes (Mg-Px) (Cahill et al., 2009; Klima, Pieters, et al., 2011; Moriarty et al., 2013; Nakamura et al., 2009; Pieters et al., 2001; Tompkins & Pieters, 1999). The pervasive nature of these Mg-pyroxene-rich materials across the basin suggests that they are a result of SPA formation, either as impact melt (e.g., Nakamura et al., 2009; Vaughan & Head, 2014) or excavated materials from the lower crust and/or upper mantle (Blewett et al., 1999; Klima, Dyar, & Pieters, 2011; Lucey et al., 1998; Moriarty & Pieters, 2016c; Ohtake et al., 2014; Pieters et al., 2001). In an ~700 km region near central SPA, surface materials exhibit a more Ca-rich pyroxene composition (Moriarty & Pieters, 2016b; Ohtake et al., 2014). This unusual region is discussed in more details below.

In addition to the pervasive Mg-pyroxenes across SPA, local areas exhibiting mare/cryptomare basaltic signatures are well defined within the basin (Nelson et al., 2014; Petro et al., 2011; Pieters et al., 2001; Whitten & Head, 2014; Yingst & Head, 1999). Although it has been modeled that SPA could have melted and excavated an olivine-rich mantle (e.g., Vaughan & Head, 2014), significant olivine exposures are not observed within the SPA interior. However small, localized exposures of olivine have been observed in the central peak/peak ring structures of Schrodinger Basin and Zeeman Crater (e.g., Kramer et al., 2013; Yamamoto et al., 2012). Since these small exposures lie near the SPA exterior and are associated with extensive feldspathic material, they probably represent crustal products rather than excavated mantle cumulates. Regardless, the dominant mafic component across SPA is pyroxene.

Based on Clementine-derived estimates of Fe abundance (Lucey et al., 1998), Jolliff et al. (2000) defined two regions within SPA: an inner zone with higher Fe content (interpreted to represent excavated materials and melt) and an outer zone with lower Fe content (interpreted to represent proximal ejecta). In this analysis, we use M^3 imaging spectrometer data (Green et al., 2011; Pieters et al., 2009) to build on these general properties, defining and characterizing several distinct compositional zones across the basin.

2.2. PLC Analyses of Pyroxene Composition and Abundance

In the near infrared, spectral variations across SPA are dominated by the abundance and composition of pyroxenes (e.g., Moriarty et al., 2013; Nakamura et al., 2009; Pieters et al., 2001). These variations are reflected in the band centers and band depths of the diagnostic 1 and 2 μm spectral absorptions. For lunar pyroxenes, absorption band centers are primarily controlled by the relative abundances of Fe, Mg, and Ca in the nominally octahedral cation sites of the pyroxene mineral structure (Burns, 1993). Mg-rich orthopyroxenes exhibit the shortest-wavelength 1 and 2 μm band centers, while Ca,Fe-rich clinopyroxenes exhibit the longest-wavelength 1 and 2 μm band centers (extensively documented by Klima et al., 2007, and Klima, Dyar, & Pieters, 2011). In mixtures, absorption band depths are correlated with pyroxene abundance (as well as secondary factors such as optical maturity and Fe^{2+} content). These bands are superimposed on a spectral continuum, which for lunar surface materials is difficult to precisely model but is typically dominated by the effects of mixing and space weathering (e.g., Pieters et al., 2000).

For quantitative estimates of absorption band depths (EBDs) and the wavelength position of band centers (EBCs), we employ a fitting routine using Parabolic absorption band fitting after removing a two-part Linear Continuum (PLC) (Moriarty & Pieters, 2016b). The PLC technique, demonstrated in Figure 2 and validated by Moriarty and Pieters (2016a), is a straightforward method for identifying and characterizing compositional properties of natural pyroxene-rich materials using absorption band depths and centers. PLC is an advantageous approach in that it is computationally simple and can therefore be automated and quickly applied to large volumes of remote sensing data. This is especially useful for characterizing large regions such as SPA. Furthermore, PLC computes quantities that are directly linked to mineralogical properties, as opposed to less-direct methods than can be more difficult to interpret (e.g., PCA, band ratios, and color composites).

Essentially, PLC describes an updated approach to simple quadratic spectral characterization techniques that have been around for decades (e.g., Cloutis & Gaffey, 1991). PLC differs from existing techniques in the specifics of its fitting routine, in that several degrees of automation are available depending on the specific analysis scenario. A detailed description of the exact steps involved in PLC derivation of EBCs and EBDs for the 1 and 2 μm pyroxene absorption bands (EBC1, EBC2, EBD1, and EBD2) is given in the supporting information and is further described by Moriarty and Pieters (2016a).

A systematic, sample-based validation of compositional interpretations and limitations from PLC-derived band values is provided by Moriarty and Pieters (2016a). In brief, for pure pyroxenes, the PLC model delivers band center measurements within a few nanometer (Moriarty & Pieters, 2016a) of band center measurements obtained using the more physically realistic Modified Gaussian Model (Sunshine et al., 1990). PLC is not designed to serve as an unmixing model and is not capable of unraveling individual contributions from components such as multiple pyroxene compositions, olivine, crystalline plagioclase, glass, and ilmenite. Rather, PLC is sensitive to overall pyroxene abundance and differences in *composite* pyroxene composition. Therefore, when investigating a region where the primary spectral variations are dominated by difference in the abundance and composition of pyroxenes, PLC provides an excellent overview of compositional diversity.

2.3. Moon Mineralogy Mapper Data and Analysis

The diagnostic 1 and 2 μm pyroxene absorption bands are well resolved in M^3 data, which are the primary data evaluated in this paper. M^3 (Pieters et al., 2009) was an imaging spectrometer that flew as a guest

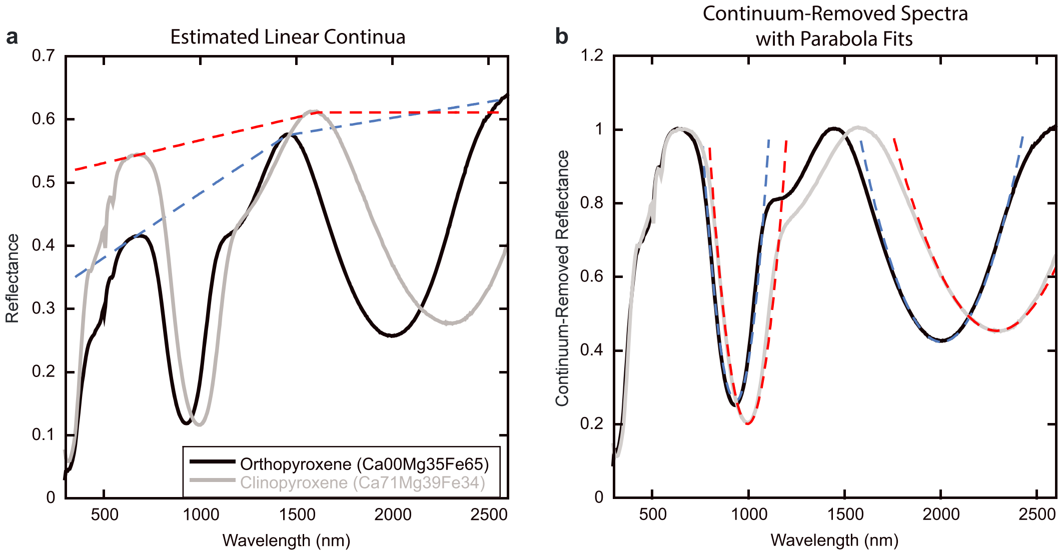

Figure 2. Example derivation of spectral parameters using an approach involving Parabolic band fits after a two-part Linear Continuum removal (PLC, discussed further in the text, supporting information, and Moriarty & Pieters, 2016a). (a) Laboratory reflectance spectra (solid) with estimated two-part linear continua (dashed) for two pure pyroxenes (orthopyroxene En35,Fs65, RELAB #DL-CMP-025; clinopyroxene En39, Fs34, Wo27, RELAB #DL-CMP-051, discussed further in Klima et al., 2007, and Klima, Dyar, & Pieters, 2011). (b) Continuum-removed spectra and parabola fits for the pure pyroxene spectra. Two diagnostic absorption band parameters are indicated: estimated band center (EBC) reflects pyroxene composition (see Figure 8), while estimated band depth (EBD) is sensitive to pyroxene abundance in a mixture.

instrument on Chandrayaan-1, the first lunar mission launched by the Indian Space Research Organization (Goswami & Annadurai, 2009). The Level 2 M^3 data used here were obtained in the instrument's global mapping mode, which offers a wavelength-dependent spectral resolution of either 20 or 40 nm (Green et al., 2011). The nominal spatial resolution in global mode was 140 m per pixel. Due to unplanned spacecraft issues, only a few measurements of the lunar surface were acquired in the "Target" instrument mode, which offered 10 nm spectral resolution at 70 m per pixel spatial resolution.

Observing conditions (such as phase angle, solar illumination, detector temperature, and spacecraft altitude) changed throughout the mission, affecting spatial resolution as well as the behavior of the detector (Boardman et al., 2011). To account for these changing conditions, M^3 data are divided into several convenient optical periods (OPs). Calibration efforts (such as a photometric correction to a standard viewing geometry; Besse et al., 2013) were undertaken to produce an approximately uniform data set, but small and often systematic differences in data quality persist between the OPs.

While M^3 achieved nearly complete coverage of SPA, the coverage of the basin is divided between several distinct OP conditions, labeled OP1A, OP1B and OP2A, OP2B, and OP2C (Boardman et al., 2011). For convenience during calibration, the M^3 team subdivided OP2C into three informal groups OP2C1, OP2C2, and OP2C3 (e.g., Besse et al., 2013). The M^3 coverage of SPA for each subperiod is shown in Figure S1. OP2C1 and OP2C2 offer the broadest coverage of SPA, while additional coverage is also available in OP1A, OP1B, OP2A, and OP2C3.

Preceding PLC analyses, a ground truth correction (Isaacson et al., 2013) was applied to Level 2 data in order to assure that M^3-measured absorption band properties fit the same framework as lunar samples. Essentially, this correction seeks to both (1) increase uniformity between M^3 spectra from different detector states and (2) improve consistency between M^3 spectra and laboratory spectra of lunar samples. The ground truth correction used consists of a small multiplicative factor affecting the strength and shape of the 1 μm band. Since the correction is small, it has the biggest effect on the spectra of well-developed soils or materials with low mafic content. For M^3 data, two multiplicative ground truth correction factors were derived: one for when the detector was "warm," another for when it was "cold" (Isaacson et al., 2013). All optical subperiods used here (except OP2C2) correspond to a single temperature state of the detector

(Lundeen et al., 2011), and the appropriate correction was applied. OP2C2 contains both warm and cold detector states. Since OP2C2 data across SPA mostly correspond to the warm detector state, the warm ground truth factor was applied to the OP2C2 mosaic (serving as an approximate correction). To ensure consistency between analyses, the ground truth correction should always be applied when working with M^3 data.

Due to the enormous size of SPA, we perform PLC analysis on M^3 global mosaics (resampled to ~1.5 km/pixel) constructed by M^3 team member Joseph Boardman (personal communication). While these global mosaics have a lower spatial resolution than individual M^3 image-cubes (by a factor of ~10), they provide an excellent overview of compositional heterogeneity across SPA. Each mosaic contains only data from a single optical subperiod. Using PLC fitting (Moriarty & Pieters, 2016b), absorption band parameter maps for the EBD (EBD1 and EBD2) and EBC (EBC1 and EBC2) were calculated for each group of M^3 data covering SPA, allowing characterization and analysis of regional trends in pyroxene composition and abundance. The band depths across SPA derived from each optical subperiod are compared in Figure S2.

As mentioned above, the M^3 instrument behaved somewhat differently in each OP, largely due to thermal issues (Boardman et al., 2011). The issues in the data persist to some extent even after ground truth (available on PDS) (Isaacson et al., 2013) and photometric corrections (as included in the Level 2 data) (Besse et al., 2013). These issues can result in slightly different values for band center and depth measurements for the same areas in different optical subperiods. These spectral differences between OPs result from many complex factors and vary with location, composition, and observation geometry, resulting in EBD values that may differ between subperiods by up to 0–20%.

The differences in instrument behavior between OPs preclude precise, quantitative compositional analysis across multiple OPs. However, relative spatial relationships within individual subperiods are unaffected and are well suited for evaluating local and regional compositional trends. Since OP2C1 offers the most complete coverage of central SPA, these analyses are grounded in OP2C1 data and supplemented with data from other OPs where necessary.

3. Results

3.1. Pyroxene Band Depths Across SPA

A map of 2 μm EBDs across SPA is provided in Figure 3. EBD1 is provided in Figure S3. EBD1 maps are similar to EBD2 maps, but exhibit slightly more noise. For discussion purposes, SPA materials can be grouped into general band depth ranges that are related to pyroxene abundance and optical maturity. These EBD2 ranges are defined below, and example spectra for each are given in Figure 4:

Strong	($EBD2 > \sim 0.1$, red/yellow in Figure 3a): optically immature pyroxene-dominated materials. These exposures are mostly confined to central SPA and are associated with fresh craters and highly sloped surfaces such as crater walls and central peaks. These materials represent the freshest exposures of pyroxene-dominated materials in SPA.
Intermediate	($EBD2 > \sim 0.05$, green in Figure 3a): relatively optically mature pyroxene-dominated materials. These materials are pervasive throughout the SPA interior and appear to represent pyroxene-rich soils and older, degraded crater structures.
Weak	($EBD2 < \sim 0.05$, blue in Figure 3a): mixed mafic/feldspathic materials. These materials are prevalent in the outer reaches of the SPA interior and probably represent feldspathic materials with a small but nonzero mafic component, likely the result of mixing between mafic and feldspathic materials.
Featureless	($EBD2 \sim 0$, purple/colorless in Figure 3a): highly feldspathic materials. These materials exhibit no detectible mafic minerals and appear highly feldspathic in nature. They are common throughout the rim and exterior of SPA.

Although absorption band strength can be used as a first-order proxy for pyroxene abundance, it alone cannot fully characterize the range of pyroxene diversity across SPA. To further evaluate the mineralogical diversity within the basin, absorption band centers (which are diagnostic of pyroxene composition) are discussed in the following section.

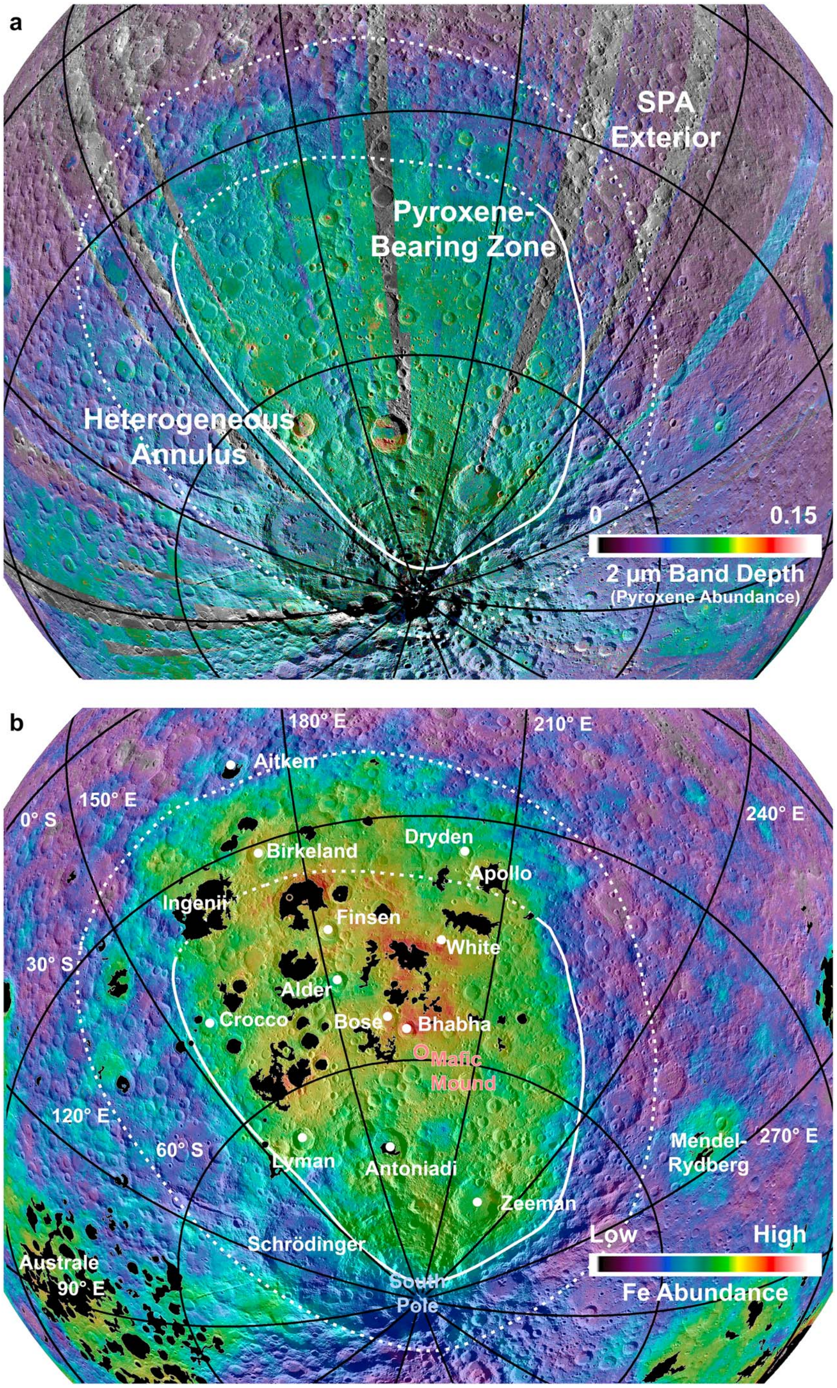

Figure 3. (a) A composite 2 µm band depth map for the SPA region incorporating M^3 data from all optical periods. (b) Iron abundance measured by Lunar Prospector (Lawrence et al., 2002). In (b), the locations of known mare basalts are shown in black (as mapped by Scott & McCauly, 1977; Stuart-Alexander, 1978; Wilhelms & El-Baz, 1977; Wilhelms et al., 1979; and Nelson et al., 2014). To first order, absorption band depths in (a) reflect pyroxene abundance, and therefore the central region of SPA exhibits uniformly elevated pyroxene abundance compared to surrounding areas. This pyroxene-bearing zone is demarcated with solid lines where strong band depths are closely correlated with Fe enrichment in the Lunar Prospector data. The northernmost boundary of the pyroxene-bearing zone is demarcated with a dashed line where there is less correlation (due to factors discussed in the text). Exterior to the pyroxene-bearing zone, localized nonmare pyroxene-rich deposits are interspersed with more feldspathic materials. This heterogeneous annulus is demarcated with the outer dashed line. Beyond this heterogeneous annulus, nonmare materials are primarily feldspathic in nature and represent the anorthositic crustal materials of the SPA exterior.

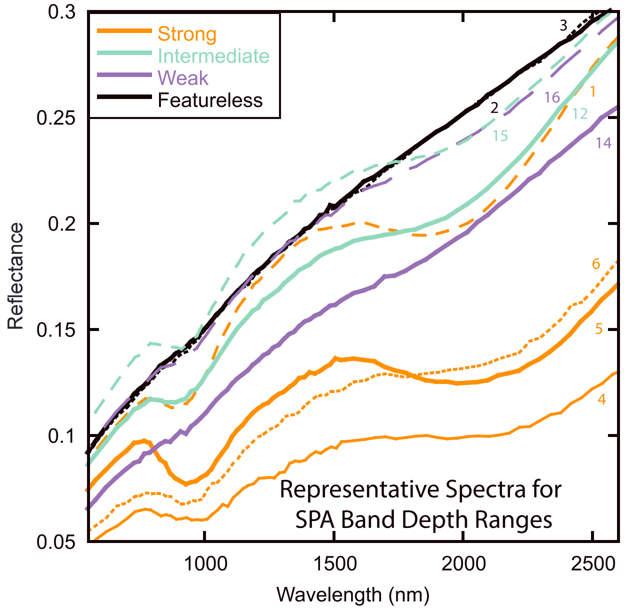

Figure 4. Representative M^3 spectra for different measured estimated band depth (EBD) ranges observed across SPA. These spectra are 3 × 3 pixel averages from M^3 global mode data and were obtained from the numbered locations detailed in Table S1. Spectra were obtained from small, fresh craters or steep slopes in order to minimize the effect of optical maturity on band strengths. "Strong" spectra exhibit EBD > 0.1. "Intermediate" spectra exhibit EBD > 0.05. "Weak" spectra exhibit EBD < 0.05. Featureless spectra lack 1 and 2 μm absorption bands.

3.2. Pyroxene Band Centers Across SPA

Since pyroxene absorption band centers are inherently linked to composition (Burns, 1993; Klima et al., 2007; Klima, Dyar, & Pieters, 2011), we derive and map band center values via the PLC technique to evaluate compositional relationships across the basin. Figure 5 presents a compositional overview of central SPA using the mineralogically sensitive 1 (Figures 5a and 5b) and 2 μm (Figure 5c) absorption band centers.

The band center maps of Figure 5 highlight the character and extent of compositional diversity of pyroxenes across SPA. In these maps, materials with 1 and 2 μm bands at relatively long wavelengths (indicating Ca, Fe-rich pyroxenes) appear yellow/red, while materials with short-wavelength 1 and 2 μm absorption bands (Mg-rich pyroxenes) appear purple/blue. Materials with 1 and 2 μm bands at intermediate wavelengths appear green/yellow. These band center relationships are used to evaluate the spatial distribution of pyroxene compositions across SPA in the following sections. Spectra for several example compositions are given in Figure 6. Spectra were collected from locations itemized in Table S1. To minimize the spectral contribution from mature soils, spectra were collected from fresh craters and steeply sloped surfaces.

4. Discussion and Integration

4.1. Identification of Distinct Compositional Zones

Band depth and band center measurements of South Pole-Aitken surface materials reveal regular patterns of compositional diversity across the basin. Integrating these measurements provides an overview of spatial relationships between pyroxene abundance and composition. From the band depth and band center maps given in Figures 3 and 5, several distinct compositional zones are evident. The extent and properties of these zones are discussed in the following sections.

4.1.1. Spatial Insights From Pyroxene Abundance Across SPA

As seen in the PLC-derived band depth map (Figure 3a), the SPA interior exhibits a broad region with fairly uniform strong absorption bands, implying elevated pyroxene abundance. This "pyroxene-bearing zone" is over 1,000 km in diameter and exhibits relatively homogeneous enhanced pyroxene abundance among craters of a variety of sizes, from small surficial craters (<1 km in diameter) to the walls, peaks, rings, floors, and ejecta of larger impact structures such as Lyman (84 km), Antoniadi (143 km), and the southern portion of Apollo Basin (538 km).

The boundaries of the pyroxene-bearing zone are naturally correlated with elemental Fe abundance as measured by Lunar Prospector (Figure 3b). However, elevated Fe abundance persists further to the north than the M^3-identified pyroxene-bearing zone. Some of the Lunar Prospector signal clearly results from the presence of local mare basalts in the region (see mapped distribution in Figures 3b and 5b). The spatial difference between Lunar Prospector FeO and M^3 data should be noted, but some of these differences probably arise from differences in spatial resolution between data sets.

Small, localized regions of more feldspathic materials are present in the northwest quadrant of the pyroxene-bearing zone (purple/blue pixels in Figure 3a). For example, the central peak and southeast rim of Alder (77 km) is relatively feldspathic in nature, as identified by weak-to-nonexistent pyroxene absorption bands. Since this material exhibits very weak 1 and 2 μm absorptions, it is thought to represent lunar plagioclase, either highly shocked or possibly containing very low FeO since the plagioclase 1.3 μm absorption is not evident (Cheek et al., 2011; Pieters, 2017). Such featureless feldspathic material is dominant outside of the pyroxene-bearing zone, where the abundance of mafic materials decreases substantially.

As can be inferred from Figure 3a, the region directly outside the pyroxene-bearing zone exhibits feldspathic materials heterogeneously interspersed with localized nonmare pyroxene-bearing deposits. This patchwork of mafic and feldspathic materials is observed across the surface as well as crater structures of a variety of sizes. Notably, this trend is not limited to the Lunar Prospector Fe-enriched zone (Figure 3b), as similar combinations of lithologies are observed adjacent to the entire pyroxene-bearing zone. This region of spatially interspersed feldspathic and mafic materials is defined as the "heterogeneous annulus." Spectral parameter maps and example spectra for a subset of this region demonstrating these heterogeneous trends are given in Figure 7. Outside of the heterogeneous annulus, the "SPA exterior" exhibits primarily feldspathic materials (apart from localized mare basalts). The compositional boundary between the heterogeneous annulus and SPA exterior is uncertain in the South Polar region due to the more challenging illumination conditions, leading to nosier M^3 data.

4.1.2. Spatial Insights From Pyroxene Composition Across SPA

The pyroxene-bearing zone can be further divided into two compositionally distinct regions based on differences in observed band centers (Figure 5), reflecting the spatial extent of pyroxene compositions across SPA. Most of the SPA interior exhibits short-wavelength pyroxene bands (blue in Figures 5a–5c) except for an ~700 km irregularly shaped region in the center of the pyroxene-bearing zone. This central area exhibits distinctive pyroxene compositions, with band center wavelengths intermediate between mare basalts and the Mg-pyroxene-bearing materials observed elsewhere. This indicates the dominant presence of pyroxenes intermediate in Ca,Fe content. These intermediate Ca,Fe pyroxene materials appear green in Figure 5. In Figure 6, representative spectra for these intermediate compositions are compared to spectra of local mare basalts and the more common Mg-pyroxene-bearing materials.

The central region of the pyroxene-bearing zone dominated by intermediate pyroxene compositions is defined as the SPA compositional anomaly (SPACA), due to the fact that its pyroxenes differ significantly

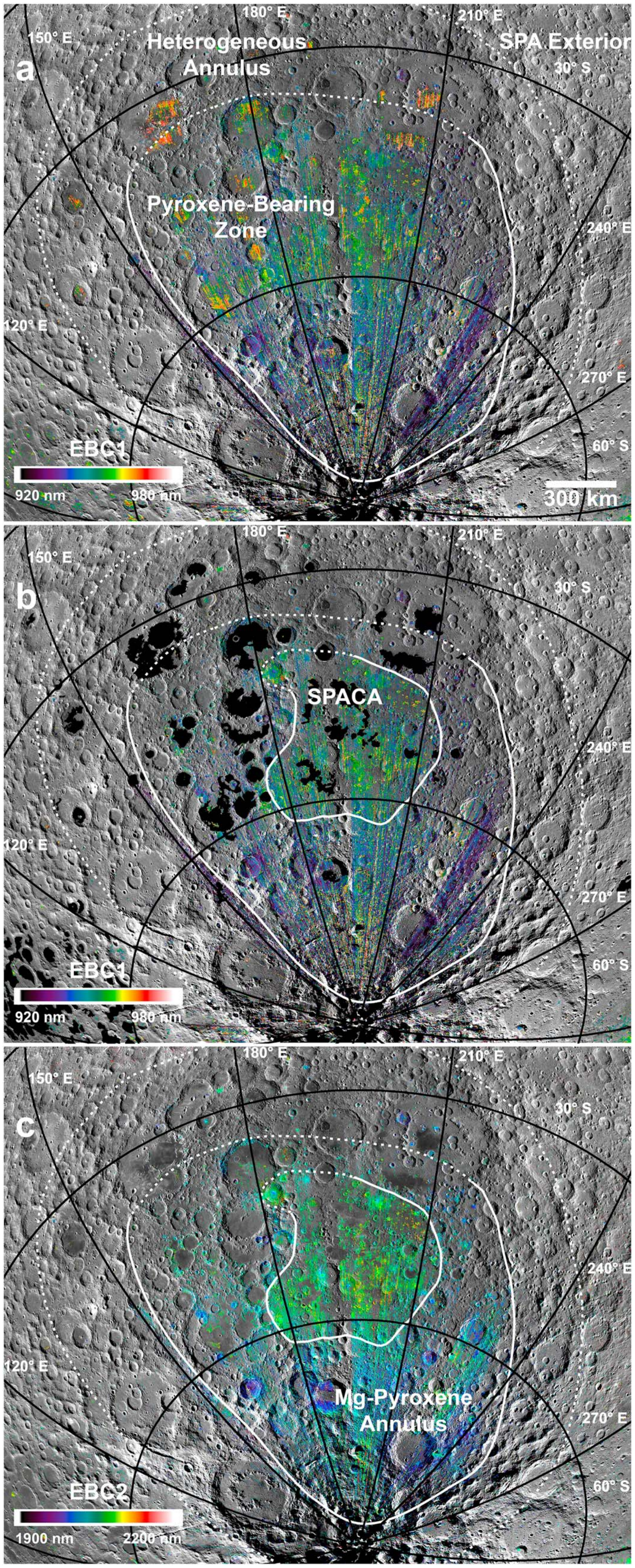

Figure 5. Maps of pyroxene absorption band centers (illustrating diversity in pyroxene composition) derived from M^3 data using the PLC technique. The boundaries of the pyroxene-bearing zone (Figure 3) are superimposed. Color values represent the wavelengths of absorption bands (for areas with band depths ≥0.1). These values are superimposed on an LROC WAC (Robinson et al., 2010) mosaic. In general, shorter wavelengths (blue) indicate that the surface is dominated by Mg-rich pyroxenes, while longer wavelengths (red) indicate the presence of more Ca,Fe-rich pyroxenes. (a) Wavelength of the 1 μm band center. (b) Same as (a), with known mare basalts shown in black (as mapped by Scott & McCauly, 1977; Stuart-Alexander, 1978; Wilhelms & El-Baz, 1977; Wilhelms et al., 1979; and Nelson et al., 2014). (c) Wavelengths of the 2 μm band center for the same areas, illustrating similar spatial relationships. Band center values from the known mare basalt areas have been removed to highlight nonmare compositions. (b) and (c) illustrate that the distribution of nonmare materials across the pyroxene-bearing zone is heterogeneous. Within the central region, pyroxene compositions are distinctly richer in Ca,Fe. The approximate boundaries of this central SPA compositional anomaly (SPACA) are given. The remaining area of the pyroxene-bearing zone exhibits extensive Mg-rich pyroxenes and is defined as the Mg-pyroxene annulus. Since the PLC band center measurements (parabola fits) for strong absorption bands are more reliable than those for weaker absorptions (due to a higher signal-to-noise ratio), only values for measured EBD band depths ≥0.10 are displayed (for A–C). Although PLC is capable of deriving reliable band center and depth values from spectra with weaker absorption bands, the proportion of unreliable band fits affected by spectral artifacts can be higher for these weaker bands, so for parameter maps it is useful to filter these out.

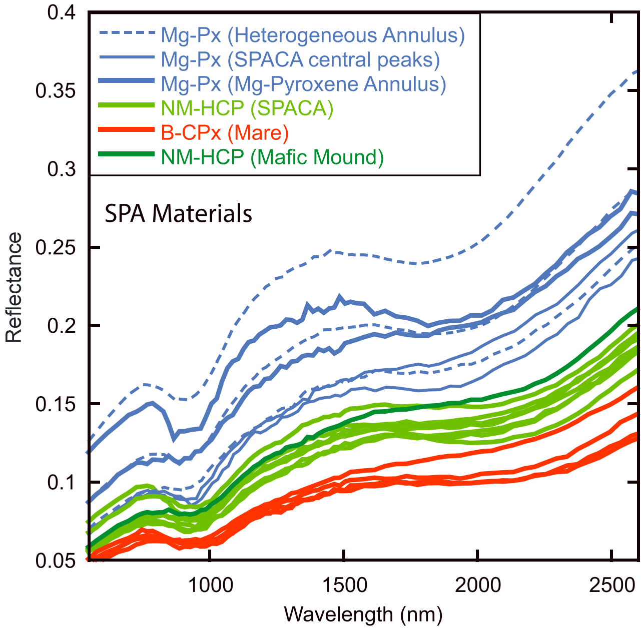

Figure 6. Example spectra for diverse pyroxene-bearing materials from across SPA (Mg-Px-CPx, NM-HCP-CPx, and B-CPx). Spectra of Mg-Px-bearing materials are further characterized based on their location (SPACA, Mg-pyroxene annulus, and heterogeneous annulus). Spectra of NM-HCP-bearing materials include SPACA materials as well as the unique Mafic Mound (Moriarty & Pieters, 2015). Spectra of B-CPx materials are from known mare basalts. Spectra are 3 × 3 pixel averages from M^3 global mode data and were obtained from locations detailed in Table S1.

from those elsewhere in SPA (and are therefore "anomalous," other than some mare basalt mixtures and uncertain pixels near polar latitudes). Throughout the remainder of the pyroxene-bearing zone, materials are dominated by distinctly more Mg-rich pyroxenes exhibiting shorter-wavelength 1 and 2 μm band centers. Henceforth, we refer to the zone surrounding the SPACA region of the pyroxene-bearing zone as the Mg-pyroxene annulus.

SPACA is centrally located within SPA and is associated with the deepest portion of the basin. The precise boundaries of SPACA are somewhat obscured by superimposed impact craters, impact-driven mixing, and later mare basalts. However, the approximate boundaries of SPACA can be established using the following criteria: (1) fairly long-wavelength 1 and 2 μm absorption bands (Figure 5) and (2) intermediate brightness across the M^3 spectral range (generally brighter than typical mare basalts, but darker than highlands or Mg-bearing materials; see Figure 6). SPACA appears to also exhibit a relatively crater-deficient terrain (Head et al., 2010; Kadish et al., 2011; Moriarty & Pieters, 2016b). Although highly irregular in shape, SPACA spans ~750 km north to south and ~650 km east to west. It includes the unusual "Mafic Mound" described by Moriarty and Pieters (2015).

Exterior to the Mg-pyroxene annulus of the pyroxene-bearing zone, mafic materials are much less abundant and are heterogeneously mixed within more widespread feldspathic areas. As seen in Figures 5 and 7, most nonmare pyroxene exposures within the heterogeneous annulus, although often highly localized, are dominated by Mg-rich pyroxenes.

4.2. Compositional Inferences

4.2.1. Context From Lunar Samples and Pure Pyroxenes

Well-characterized lunar samples (and other laboratory-measured materials) are crucial for accurate compositional interpretations of lunar surface materials observed remotely. Here we provide the context for compositional interpretations across SPA based on integrated laboratory analyses of lunar and pure pyroxene samples. PLC-derived band centers of SPA materials (from M^3 data) are integrated with comparable PLC-derived band centers of several laboratory-measured lunar samples with well-defined compositions, as well as pure pyroxene samples covering a range of compositions. These important links between sample compositions and remote sensing measurements are illustrated in Figure 8.

Three sample collections are considered here. Integrated composition and spectral analyses of lunar rocks and minerals from the Lunar Rock and Mineral Characterization Consortium (LRMCC) (Isaacson et al., 2011, and references therein) provide insight into the mineralogy and petrology of mare basalts and their relation to spectral properties. Similarly, integrated composition and spectral analyses of lunar soils characterized by the Lunar Soil Characterization Consortium (LSCC) (Noble et al., 2006; Pieters & Taylor, 2003; Taylor et al., 2001, 2010) provide insight into space weathering, mixing, and other lunar surface processes across a range of mare and nonmare compositions. Detailed compositional and spectral analyses of pure pyroxenes produced synthetically (Klima et al., 2007; Klima, Dyar, & Pieters, 2011) provide important insight into the wide range of pyroxene compositions possible on the Moon.

The relationship between band centers and compositions for the suite of pure pyroxenes (small circles) is illustrated in Figure 8. The systematic trends between pyroxene composition and band centers is illustrated in Figures 8a and 8b. Band centers for the pure pyroxenes are compared to those for the LSCC soils and LRMCC rocks in Figure 8b. Pure pyroxene compositions and average pyroxene compositions for several LRMCC basaltic rocks and LSCC soils are compared in Figure 8c.

It is important to note that each individual sample from the LRMCC and LSCC collections contain a range of pyroxene components resulting from several natural factors such as cooling history, mineral exsolution, and

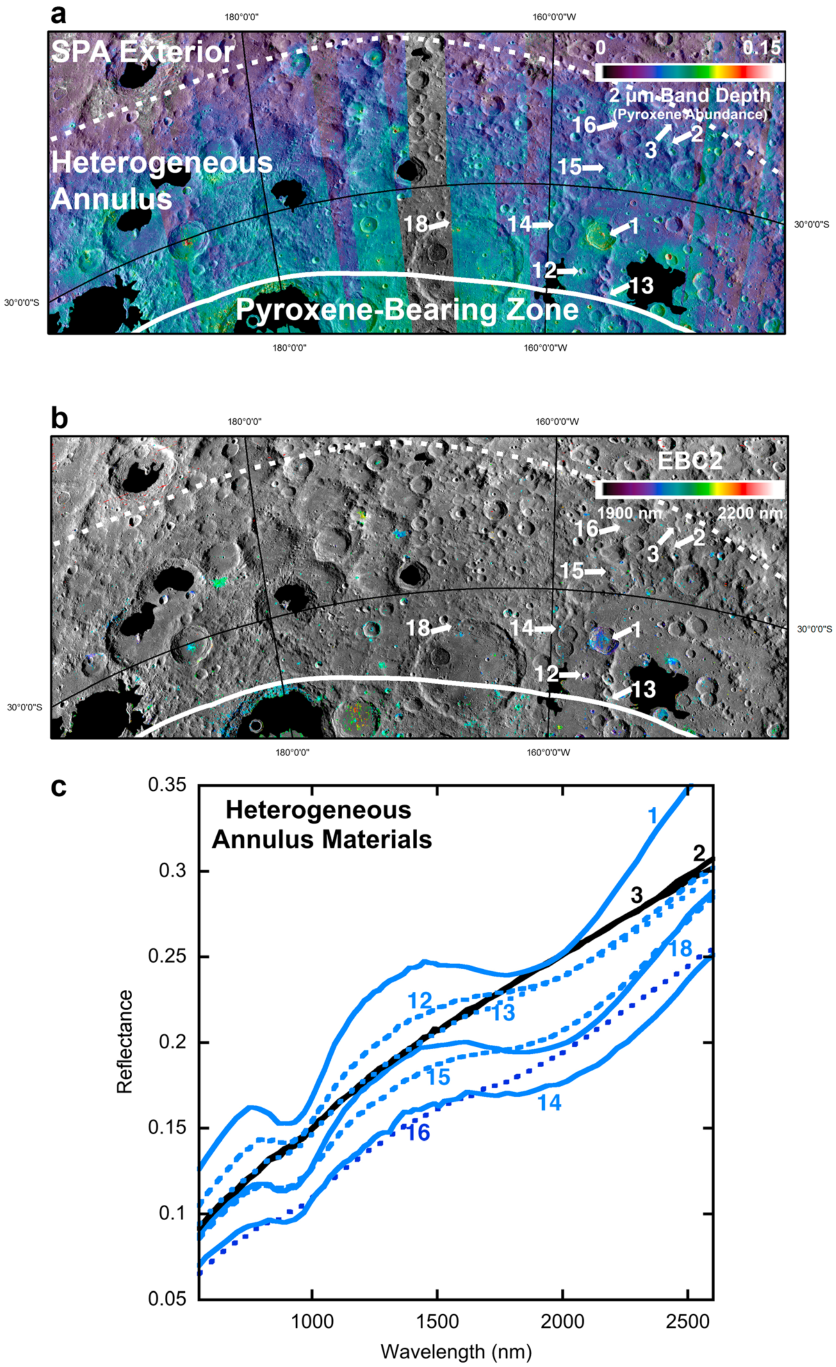

Figure 7. (a and b) PLC parameter maps of the northern portion of the heterogeneous annulus. Known mare basalts are shown in black. (a) Relative pyroxene abundance map (detail of Figure 3a, EBD2). (b) Pyroxene composition map (detail of Figure 5c, EBC2). (c) Example spectra illustrating the diverse nature of heterogeneous annulus materials, including a preponderance of Mg-pyroxenes interspersed with more highly feldspathic materials. Spectra numbers correspond to detail specified in Table S1. Spectra are derived from 3 × 3 pixel averages in M^3 global-mode data and were obtained from small, fresh craters or steeply sloped areas in order to minimize the effects of optical maturity.

physical mixing (for breccias and soils). As emphasized by Moriarty and Pieters (2016a), band center values from remote sensing data represent composite absorption bands resulting from highly complex, nonlinear mixtures of many pyroxene and nonpyroxene components. While the relationship between pure pyroxene compositions and band centers is well established by crystal physics (Burns, 1993; Klima et al., 2007; Klima, Dyar, & Pieters, 2011), natural materials are inevitably mixtures whether they be a pristine rock,

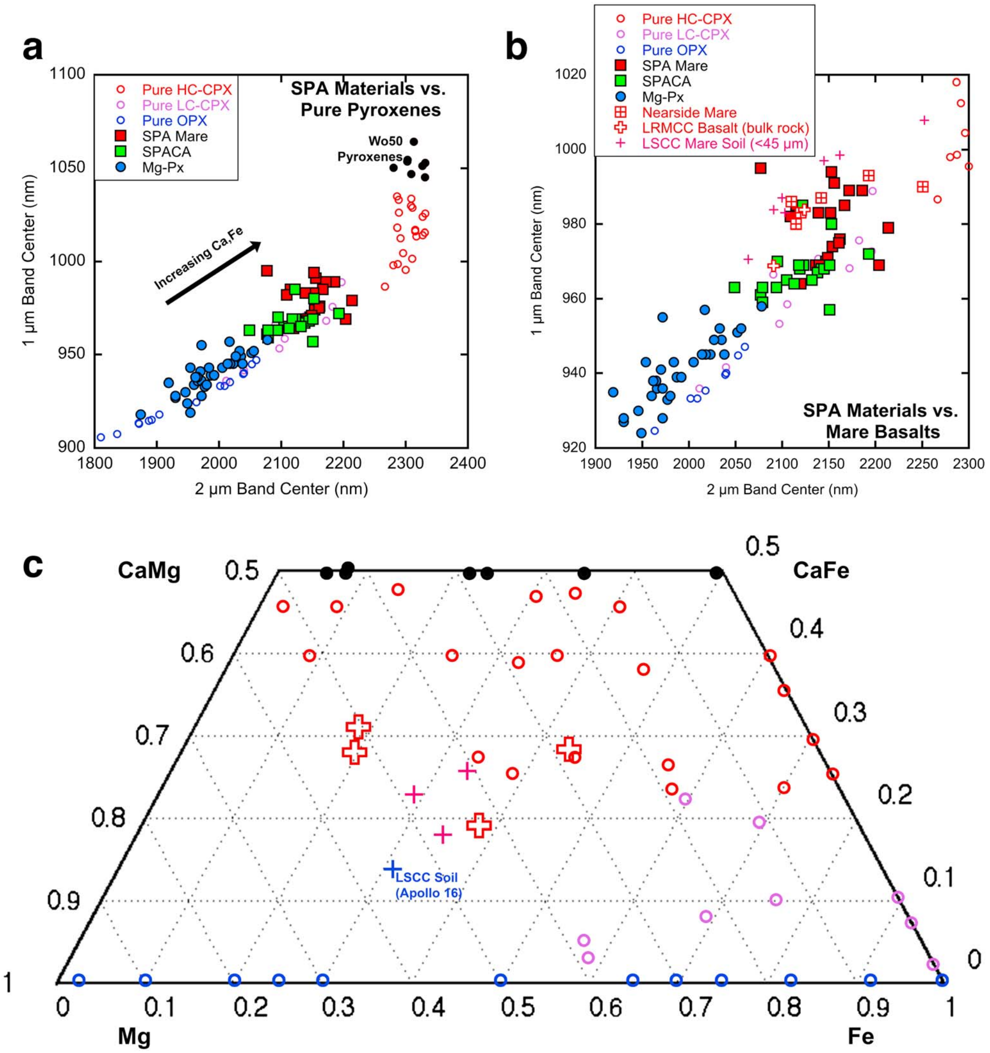

Figure 8. Pyroxene compositional relationships between SPA materials (filed blue, green, and red symbols), lunar samples (plusses), and pure pyroxenes (small open or black circles). Wo50 pure pyroxene compositions (not common on the Moon) are shaded black. (a) PLC-derived 1 µm band center versus 2 µm band center values for SPA mare basalts, Mg-pyroxene-bearing materials, and SPACA materials in the context of pure pyroxenes (Klima et al., 2007; Klima, Dyar, & Pieters, 2011). Note that the pure pyroxenes exhibit an upturn at long wavelengths, as the 2 µm band center reaches maximum wavelength of ~2,300 nm at moderate-to-high- Ca content (while the 1 µm band continues to shift to longer wavelengths with increasing Ca content) (Klima, Dyar, & Pieters, 2011). As in Figures 4 and 6, band center values for SPA materials were obtained from small, fresh craters or steep slopes in order to capture the compositional properties of local materials, rather than well-developed soils. (b) Same data as (a) with an expanded scale to emphasize band center trends among natural materials. The remote sensing and pure pyroxene data have been supplemented with band center values for several LRMCC basaltic rocks and LSCC soils measured in the laboratory (Isaacson et al., 2011; Noble et al., 2006; Taylor et al., 2001, 2010). Rocks include Apollo 15 low-Ti at coarse and fine grain size fractions. Soils include several individual <45 µm bulk grain size samples from Apollo 11, 15, and 17. M^3-measured band center values for small craters near the Apollo 15 landing site are also included, serving as a bridge between lunar samples and SPA mare. (c) Average pyroxene compositions measured for pure pyroxenes, as well as several LRMCC lunar rocks (two samples each from Apollo 15 and 17) and LSCC lunar soil samples (Apollo 11, 15, 16, and 17). These average pyroxene compositions are derived from the individual Fe,Mg,Ca content of several diverse pyroxene components identified within each sample, weighted by the abundances of each pyroxene component (Isaacson et al., 2011; Noble et al., 2006; Taylor et al., 2001, 2010).

well-developed soil, or surface swaths measured via remote sensing. Other natural processes such as space weathering affect band depths but are not known to affect band centers (e.g., Pieters et al., 2000). Therefore, all such spectra arise from a highly complex and nonlinear suite of both compositional and noncompositional factors.

PLC analyses can only provide a single band center and depth value for each absorption band measured. This provides an overview of *composite* pyroxene properties, rather than singling out specific individual components. Therefore, the most relevant compositional quantity for interpreting PLC band center values is the *composite* pyroxene composition. For the most appropriate framework for comparison, Figure 8c presents the average pyroxene compositions for several LSCC and LRMCC samples, calculated from the measured compositions and abundances of the pyroxene components within each sample (i.e., a weighted average of the Fe,Mg,Ca abundance in each pyroxene component present).

As shown by Moriarty and Pieters (2016a), PLC band center measurements are indeed sensitive to *composite* pyroxene composition for the LRMCC rocks and LSCC soils. Band centers for these samples exhibit a relationship to average pyroxene composition following the relationships observed with pure pyroxenes, as the 1 and 2 μm band centers for these materials occur at longer wavelengths for samples with higher Fe,Ca. This validates the PLC approach for interpretation of lunar surface materials observed remotely. Although PLC cannot identify individual pyroxene compositions, it is a useful tool for evaluating overall pyroxene diversity across a region.

Figure 8 also links spectral properties of SPA surface materials at sampled sites (as measured by M^3) to spectral properties of known pyroxene-bearing samples. Sampling locations were chosen from well-illuminated areas with reliable spectral fits, avoiding unreliable values caused by spectral artifacts. In Figure 8b, PLC-derived band centers from M^3 spectra of small mare craters near the Apollo 15 sample site are included for comparison. These remotely acquired band centers are comparable to the laboratory-measured band centers of the LRMCC rocks and LSCC mare soils from the Apollo 11, 15, and 17 regions. This bridge between lunar samples and remote sensing measurements further validates the reliability of M^3 PLC-derived band centers in the context of pyroxene compositional analyses.

4.2.2. Compositional Assessment of SPA Materials

Several spectral differences between SPA mafic materials are immediately apparent in Figure 6. Mare basalts exhibit the lowest overall reflectance, while the Mg-pyroxene-rich materials exhibit the highest reflectance. SPACA surface materials exhibit intermediate reflectance but are more similar to Mg-pyroxene-rich materials than mare basalts.

PLC-derived band centers for diverse SPA materials measured by M^3 are further compared in Figures 8a and 8b. These data include a representative sampling of SPA mare basalts, Mg-pyroxene-rich materials, and SPACA surface materials. The Mg-pyroxene-rich materials, which have the shortest-wavelength 1 and 2 μm band centers, are pervasive. Mare basalts, which exhibit the longest-wavelength 1 and 2 μm band centers, are more localized. The unusual SPACA surface materials exhibit band centers at somewhat shorter wavelengths than that of mare basalts, but with an overlapping distribution.

As seen in Figure 8a, the band center range of SPA materials extends over only a portion of the full range observed for pure pyroxenes and appears to exclude lithologies dominated by very high-Ca clinopyroxene and very Mg-rich orthopyroxenes. This does not preclude the presence of these minerals within SPA, but rather suggests that the *average* pyroxene compositional range falls well within these extremes.

Although SPA surface materials are necessarily mixtures, distinct spatial variations and band center trends are clearly observed and can be used with a priori geologic context and laboratory analyses of samples to make compositional distinctions and inferences. By integrating these analyses, three general pyroxene-bearing compositional types across SPA are defined. These are identified largely by the dominant pyroxene composition present:

i. Basaltic clinopyroxene (B-CPx): In Figure 5, these materials appear red/yellow, corresponding approximately to 1 μm band centers >980 nm and 2 μm band centers >2,100 nm. Most exposures of these materials also exhibit relatively low reflectance in M^3 data. As seen in Figure 8b, mare basalts in SPA exhibit similar band centers to nearside mare and basaltic samples, indicating similar average pyroxene compositions. Through laboratory analysis of returned samples, the average pyroxene compositions of mare materials are fairly well defined, although individual pyroxene components span a wide range of compositions (Isaacson et al., 2011). Several example average mare pyroxene compositions are presented in Figure 8c. SPA mare exhibit a very similar range in band centers as the nearside mare and basaltic samples, and therefore have a very similar range of average pyroxene compositions. Therefore, we interpret the dominant mafic mineral in SPA mare to be clinopyroxene, similar to the basaltic lunar samples.

ii. Nonmare high-Ca,Fe pyroxene (NM-HCP): In Figure 5, these materials appear green/yellow, corresponding to 1 μm band centers >960 nm and 2 μm band centers >2,050 nm. NM-HCP pyroxenes are the dominant mafic component of SPACA surface materials. As shown in Figures 8a and 8b, SPACA materials exhibit somewhat shorter-wavelength band centers than mare basalts, but with some overlap in the distributions. Performing Welch's unequal variance *t* test on the 1 μm band centers for SPACA materials and SPA mare basalts results in a *P* value of less than 0.0001, indicating that the difference in band centers for these materials is highly statistically significant. The somewhat shorter-wavelength band centers imply that the range of NM-HCP pyroxene compositions is somewhat lower in average Ca (or Fe) content than B-CPx. In the pyroxene composition quadrilateral of Figure 8c, the range in average pyroxene compositions for SPACA NM-HCP materials is therefore inferred to be slightly below and/or to the left of the B-CPx range (representing slightly lower Ca/Fe content). Furthermore, the NM-HCP materials are significantly brighter than B-CPx materials (Figure 6), indicating an overall different mineralogy. The petrological character and origin of these unusual NM-HCP materials are uncertain, and they likely represent either (1) a mixture of B-CPx compositions, Mg-pyroxenes, and other crustal materials or (2) a distinct igneous rock type (Moriarty & Pieters, 2015, 2016a).

iii. Mg-rich pyroxene (Mg-Px): These nonmare materials appear blue/purple in Figure 5, indicating 1 μm band centers <960 nm and 2 μm band centers <2,050 nm. Mg-Px materials are pervasive throughout the Mg-pyroxene annulus and appear locally within the heterogeneous annulus and within several central peaks across SPACA. Due to their average short-wavelength band centers, Mg-Px materials are inferred to be dominated by Mg-rich pigeonites and orthopyroxenes. The most likely range of average pyroxene compositions is significantly below and to the left of the mare basalt range in Figure 8c, shifted toward the Mg end-member.

These three compositional groups are based on inferred pyroxene composition and do not account for other factors such as plagioclase or opaque abundance. Although each is distinct, this grouping alone cannot specify which are impact melt, impact breccias, or preimpact basement materials. Nevertheless, these groups identify and partially characterize distinct spatially coherent lithologies across SPA, such as mare basalts (B-CPx), SPACA surface materials (NM-HCP), and Mg-rich pyroxenes found throughout SPA.

4.3. The Near-Surface Compositional Zones of the South Pole-Aitken Basin

An integrated graphical representation of the compositional diversity across SPA is illustrated in Figure 9. This includes PLC-derived band center information from M^3 data (comparable to that of Figure 5c) superposed on Lunar Orbiter Laser Altimeter topography. Additionally, a schematic compositional interpretation for components of major post-SPA impact craters (listed in Table 1) is superimposed. For each impact structure, representative absorption band centers and depths were derived for key features such as crater rims, walls, and central peaks. The schematic representation constructed in this way provides a simplified regional overview of compositional trends for this gigantic basin.

Although each of the four distinct compositional zones within SPA results from a complex history, the properties of each are distinct and summarized as follows:

1. SPACA: SPACA is an approximately ~700 km unit located in the central portion of SPA. It exhibits a pervasive elevated pyroxene abundance, and the surface composition is dominated by an unusual intermediate-Ca,Fe pyroxene composition (NM-HCP), distinct to both mare basalts and Mg-Px. This NM-HCP is observed at structures such as Mafic Mound (Moriarty & Pieters, 2015); the walls of Finsen, Bhabha, Bose, White, and Stoney; and the central peaks of White and Stoney. However, several large complex craters within SPACA (Bhabha, Finsen, and Stoney) exhibit distinctly Mg-rich pyroxenes in their central peaks. Since central peaks represent the deepest material exposed in any given crater (Cintala & Grieve, 1998), this suggests the presence of Mg-Px at depth, underlying the surface NM-HCP.
2. Mg-pyroxene annulus: The Mg-pyroxene annulus surrounding SPACA also exhibits an elevated pyroxene abundance, but the pyroxene composition is dominated by Mg-rich pyroxene (Mg-Px) rather than NM-HCP. The Mg-pyroxene annulus lies directly outside of the SPACA and represents the remainder of the prominent pyroxene-bearing zone (~1,000 km across in total). Mg-Px dominates crater structures over a wide range of crater sizes, indicating the presence of laterally and vertically extensive Mg-Px-bearing materials.

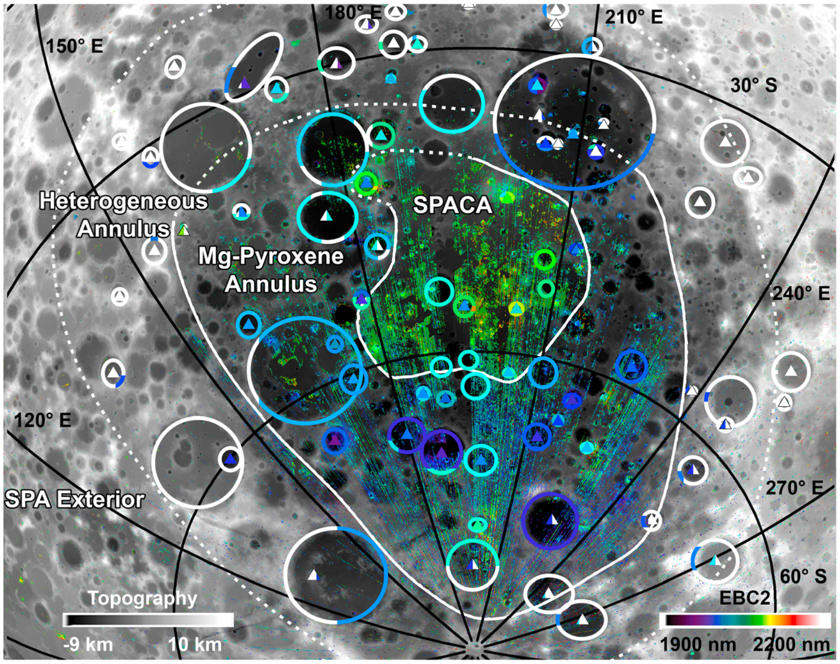

Figure 9. Summary schematic of the four distinct compositional zones within SPA, as revealed by M^3 spectral data. PLC-derived 2 μm absorption band center (EBC2) for regions with strong absorptions (EBD > 0.1) is overlaid on LOLA topography (Smith et al., 2010). Known mare basalts have been masked in order to emphasize compositional heterogeneity in nonmare materials. The superposed colored symbols (ellipses and triangles) highlight the compositional diversity inferred across a suite of large impact structures (see Table 1). The color of these symbols corresponds to general absorption band center information and reflects the dominant pyroxene compositions (if any) observed across the crater structures. The blue/purple colors indicate Mg-pyroxenes; the green/red colors indicate Ca,Fe-pyroxenes. The white indicates the presence of feldspathic materials exhibiting a lack of a mafic signature. Multiple colors are used where significant heterogeneity is observed. The ellipses correspond to crater rims and walls, while the triangles correspond to central peaks of complex craters.

3. Heterogeneous annulus: The heterogeneous annulus is associated with the outer reaches of SPA interior. It is dominated by feldspathic materials but exhibits localized pyroxene-bearing areas and a variable but typically small mafic component in soils. In general, any nonmare mafic materials found within the heterogeneous annulus are dominated by Mg-pyroxene.
4. SPA exterior: Other than isolated mare basalts, the SPA exterior is highly feldspathic and appears mafic-free.

4.4. Key Unanswered Questions

Having established the boundaries and average pyroxene compositions of these four compositional zones across SPA, several pertinent questions are raised, each meriting further analysis:

4.4.1. What is the Origin of the Mg-Rich Pyroxenes Observed Throughout South Pole-Aitken?

Mg-Px is widespread throughout SPA, occurring (a) pervasively throughout the Mg-pyroxene annulus, (b) as the dominant mafic component throughout the heterogeneous annulus, and (c) in exposures uplifted from depth within SPACA. Clearly, these Mg-Px exposures represent pervasive and deep-seated materials exposed by the massive basin-forming impact, probably as both impact melt and impact breccia. As suggested by the extensive Mg-Px exposures across SPA, these materials were probably the primary material melted and ejected during SPA formation. It should be stressed that olivine was not observed in significant abundance anywhere in central SPA, in agreement with recent targeted searches (Yamamoto et al., 2012). Considering this lack of olivine but abundance of Mg-rich pyroxene, several questions arise concerning the role of South Pole-Aitken as an important probe to the lunar interior. Are these Mg-Px materials representative of the lunar crust and/or lower mantle? What level of compositional and textural heterogeneity exists within the suite of Mg-Px materials? Is this diversity characteristic of the SPA target materials, or is it a result of processes such as impact melting, melt differentiation, and mixing? Addressing these questions can solidify the role of South Pole-Aitken as an important probe into the lunar interior.

Table 1
Large Impact Structures in the SPA Region

Crater[a]	Latitude	Longitude	Diameter (km)	Stratigraphic age[b]	Morphology[c]	M^3 Coverage[d]
Aitken	16.6° S	173.3° E	138	Upper Imbrian	CPC	OP2C1*, OP2C2
Alder	48.6° S	177.4° W	82	Lower Imbrian	CPC	OP1A*, OP2C1, OP2C2
Antoniadi	69.2° S	173.1° W	138	Upper Imbrian	Basin	OP2C1*, OP2C2
Apollo	36.0° S	152.1° W	524	Pre-Nectarian	Basin	OP2A*, OP2C1*, OP2C2
Ashbrook	81.0° S	109.0° W	158	Pre-Nectarian	Crater	OP1B, OP2A, OP2C1, OP2C2, OP2C3
Baldet	53.3° S	151.96 w	56		Crater	OP2A, OP2C1, OP2C2
Barringer	28.2° S	150.5° E	67	Nectarian	CPC	OP2C1
Bellinsgauzen	60.7° S	161.8° W	63	Nectarian	Crater	OP2C1
Berlage	63.2° S	163.5° W	94	Pre-Nectarian	Crater	OP2C1, OP2C2
Bhabha	55.4° S	165.4° W	66	Nectarian	CPC	OP2C1
Birkeland	30.1° S	173.9° E	84	Eratosthenian	CPC	OP1A, OP2C2
Bok	20.3° S	171.6° W	43	Eratosthenian	CPC	OP2C1
Borman	39.1° S	148.3° E	46	Lower Imbrian	CPC	OP2A, OP2C2
Borman V	37.6° S	151.3° W	28		CPC	OP2A, OP2C1, OP2C2
Bose	53.9° S	169.4° W	95	Nectarian	CPC	OP2C1*
Boyle	53.3° S	177.9° E	55	Nectarian	CPC	OP2C1, OP2C2
Buffon	40.6° S	133.6° W	106	Nectarian	CPC	OP2A, OP2C3
Cabannes	61.1° S	170.3° W	81	Pre-Nectarian	Crater	OP2C1
Cabannes M	64.3° S	170.3° W	48		CPC	OP2C1
Cabannes Q	63.5° S	174.9° W	50	Nectarian	CPC	OP2C1, OP2C2
Chaffee	39.1° S	154.6° W	52	Nectarian	CPC	OP2A, OP2C1, OP2C2
Chaffee F	38.9° S	153.0° W	36	Nectarian	CPC	OP2A, OP2C1, OP2C2
Chebyshev	33.9° S	133.2° W	179	Nectarian	CPC	OP2A, OP2C3
Cori	50.5° S	152.9° W	67	Nectarian	Crater	OP2A, OP2C1, OP2C2
Crommelin	67.4° S	148.1° W	94	Pre-Nectarian	CPC	OP2A, OP2C1*, OP2C2
Crommelin C	65.5° S	144.2° W	39	Nectarian	CPC	OP2A, OP2C2
Crookes	10.4° S	165.1° W	50	Copernican	CPC	OP1A*, OP2C1
Davisson	38.0° S	175.0° W	93	Nectarian	CPC	OP2C1, OP2C2*
Dawson	67.1° S	135.1° W	44	Lower Imbrian	CPC	OP2A, OP2C3
De Forest	77.0° S	163.0° W	56	Upper Imbrian	CPC	OP2C1
De Vries	19.7° S	176.7° W	58	Upper Imbrian	CPC	OP2C1, OP2C2
Doerfel	69.0° S	108.4° W	69	Upper Imbrian	CPC	OP1B, OP2A, OP2C1, OP2C2
Dryden	33.2° S	156.2° W	53	Upper Imbrian	CPC	OP2A*, OP2C1, OP2C2
Drygalski	79.7° S	88.4° W	163	Pre-Nectarian	CPC	OP1B, OP2A, OP2C1, OP2C2, OP2C3
Eijkman	63.2° S	142.7° W	56	Nectarian	CPC	OP2A, OP2C2*
Finsen	42.4° S	178.0° W	73	Eratosthenian	CPC	OP1A*, OP2C1, OP2C2
Fizeau	58.3° S	134.3° W	104	Upper Imbrian	CPC	OP2A, OP2C3
Grissom M	49.0° S	148.4° W	35	Lower Imbrian	CPC	OP2A, OP2C2
Hale	74.1° S	91.7° E	84	Upper Imbrian	CPC	OP2C1*
Hausen	65.0° S	88.0° W	163	Eratosthenian	CPC	OP1B, OP2A*, OP2C1*, OP2C2
Hopmann	51.0° S	159.5° E	89	Nectarian	CPC	OP1A*, OP2C1*, OP2C2*
Ingenii	33.7° S	163.5° E	315	Pre-Nectarian	Basin	OP1A*, OP2C1, OP2C2
Langmuir	36.0° S	129.0° W	92	Nectarian	CPC	OP2A*, OP2C1, OP2C3*
Leavitt	46.0° S	219.5° E	80	Nectarian	CPC	
Leavitt Z	42.7° S	139.5° W	64	Nectarian	CPC	
Leeuwenhoek	29.3° S	182.3° E	125	Nectarian	CPC	OP1A*, OP2C1, OP2C2
Leibnitz	38.6° S	179.1° E	236	Pre-Nectarian	Basin	OP1A*, OP2C1*, OP2C2
Lemaître	61.3° S	149.9° W	94	Nectarian	Crater	OP2A, OP2C21, OP2C2
Lemaître S	61.8° S	156.9° W	35	Nectarian	CPC	OP2A, OP2C1, OP2C2
Lippmann	55.6° S	114.4° W	160	Pre-Nectarian	Crater	OP1A, OP1B, OP2A, OP2C1, OP2C2, OP2C3
Lippmann L	57.5° S	112.4° W	57		CPC	OP1A, OP1B, OP2A, OP2C1, OP2C2, OP2C3
Lippmann R	57.1° S	121.4° W	36		CPC	OP1A, OP1B, OP2A, OP2C1, OP2C2, OP2C3
Lundmark	38.7° S	152.9° E	103	Pre-Nectarian	CPC	OP1A*, OP2C2*
Lundmark F	39.1° S	157.4° E	26		CPC	OP2C2
Lyman	64.9° S	162.5° E	83	Upper Imbrian	CPC	OP2C1*, OP2C2*
Maksutov	40.4° S	168.6° W	89	Upper Imbrian	CPC	
McNair	35.9° S	147.9° W	32		CPC	OP2A, OP2C2
Mendel	49.0° S	110.0° W	140	Pre-Nectarian	CPC	OP1A*, OP1B, OP2A, OP2C1, OP2C2
Mendel J	51.5° S	107.1° W	58	Lower Imbrian	CPC	OP2A, OP2C1, OP2C2
Minnaert	67.3° S	178.6° E	137	Pre-Nectarian	CPC	OP2C1, OP2C2

Table 1 *(continued)*

Crater[a]	Latitude	Longitude	Diameter (km)	Stratigraphic age[b]	Morphology[c]	M^3 Coverage[d]
Numerov	70.6° S	162.4° W	110	Nectarian	CPC	OP2C1, OP2C2*
O'Day	30.6° S	157.5° E	73	Copernican	CPC	OP2C2
Oppenheimer	35.3° S	67.0° W	201	Nectarian	Crater	OP2C1*, OP2C2*
Oppenheimer V	32.1° S	173.1° W	29	Eratosthenian	CPC	OP1A*, OP2C1, OP2C2*
Oresme V	40.9° S	165.7° E	56	Upper Imbrian	CPC	OP2C1, OP2C2
Orlov	25.8° S	174.8° w	64	Nectarian	CPC	OP2C1*, OP2C2
Paracelsus	23.1° S	163.4° E	86	Pre-Nectarian	CPC	OP1A, OP2C1, OP2C2
Pauli	44.8° S	137.2° E	95	Lower Imbrian	CPC	OP2C1
Petzval	62.7° S	110.6° W	93	Nectarian	CPC	OP1B, OP2A, OP2C1, OP2C2
Planck	57.3° S	136.4° E	320	Pre-Nectarian	Basin	OP2A*, OP2C1*, OP2C2
Plummer	24.7° S	154.9° W	68	Nectarian	CPC	OP2A, OP2C1, OP2C2
Plummer M	26.3° S	154.7° W	39	Upper Imbrian	CPC	OP2A, OP2C1, OP2C2
Poincare	57.1° S	162.7° E	346	Pre-Nectarian	Basin	OP1A*, OP2C1, OP2C2
Prandtl	59.8° S	141.4° E	88	Nectarian	CPC	OP2C1
Ramsay	40.1° S	145.1° E	61	Nectarian	CPC	OP2C1
Rumford	28.8° S	169.7° W	61	Lower Imbrian	CPC	OP1A*
Rumford A	25.2° S	169.0° W	30		CPC	
Rumford T	28.5° S	172.2° W	112	Pre-Nectarian	CPC	OP1A*, OP2C1, OP2C2*
Schrodinger	74.5° S	133.4° E	316	Lower Imbrian	Basin	OP2C1, OP2C2*
Sierpinski	27.0° S	154.6° E	67	Nectarian	CPC	OP1B*, OP2C2
Sniadecki	22.4° S	168.8° W	41	Nectarian	CPC	
Stoney	55.5° S	156.6° W	48	Nectarian	CPC	OP2A, OP2C1, OP2C2
Unnamed "A"	81.1° S	165.8° W	136		CPC	OP2A*, OP2C1, OP2C2
Unnamed "B"	24.7° S	171.9° W	61		CPC	OP1A*, OP2C1
Unnamed "C"	60.3° S	172.0° E	95		CPC	OP1A*, OP2C1*, OP2C2*
Unnamed "D"	56.5° S	171.1° E	56		CPC	OP1A*, OP2C1*, OP2C2*
Van de Graaf	27.6° S	171.9° E	246	Nectarian	CPC	OP2C1, OP2C2
Von Kármán	44.8° S	176.3° E	187	Pre-Nectarian	CPC	OP1A*, OP2C1*, OP2C2
Walker W	24.5° S	164.0° W	44		CPC	OP2C1
White	44.8° S	159.2° W	40	Upper Imbrian	CPC	OP2C1, OP2C2
Zeeman	74.8° S	135.8° W	192	Nectarian	CPC	OP2A, OP2C1*, OP2C2*, OP2C3

[a] Bold crater names indicate that these craters are represented schematically in Figure 9.
[b] Ages from Wilhelms et al. (1987).
[c] Complex craters with central peaks are abbreviated CPC.
[d] The stars indicate optical periods with limited or partial coverage.

4.4.2. What is the Nature of the Unusual SPACA Surface Materials?

As noted by Moriarty and Pieters (2015, 2016b), a large proportion of impact craters within SPACA show signs of significant modification. Additionally, there is some suggestion that SPACA exhibits a relatively low density of impact craters (Head et al., 2010; Kadish et al., 2011; Moriarty & Pieters, 2016b). Since the NM-HCP observed across SPACA seems to correspond to near-surface materials, it may be linked to an apparent resurfacing. If so, what is the source of the NM-HCP? Do these materials represent an unusual, early extrusive magma composition, perhaps resulting from the SPA impact? Are they a differentiated impact melt sheet product (e.g., Ohtake et al., 2014)? Could they be well-mixed ejecta from nearby basins, or ancient cryptomare? Extensive, well-mixed cryptomare? What is the relationship of NM-HCP materials to the enigmatic structure known as Mafic Mound (Moriarty & Pieters, 2015), where the same composition is observed? Understanding SPACA is key for unraveling the complex geologic evolution of South Pole-Aitken.

5. Conclusions

By analyzing pyroxene composition and abundance across the vast SPA, it was shown that the basin, although highly complex, exhibits regular patterns of compositional diversity. Using measurements from the M^3, a mafic-rich pyroxene-bearing interior was observed, and four distinct compositional zones were identified and characterized. The SPACA is an ~700 km region in the deepest, center-most region of SPA that exhibits an unusual, intermediate-Ca,Fe pyroxene-bearing surface composition. The remainder of central SPA is dominated by Mg-rich pyroxenes across a wide range of crater sizes and is therefore defined as the Mg-pyroxene annulus. Surrounding the Mg-pyroxene annulus is a heterogeneous annulus exhibiting many localized deposits of Mg-rich pyroxene embedded within low-mafic materials. At the outer reaches of the topographic rim of SPA (and beyond), the SPA exterior appears highly feldspathic. Compositional diversity across SPA is dominated by differences in pyroxene composition and abundance, as opposed to other minerals such as olivine.

The four distinct compositional zones identified here provide essential constraints for further characterizing and understanding the formation and evolution of SPA, as well as the evolution and structure of the early lunar crust and mantle. Each zone reflects its origin, as well as billions of years of subsequent processes. These include material melted and ejected in the basin-forming impact, eons of lunar volcanism and impact bombardment, and continuous integration of space weathering and micrometeorite impacts contributing to soil development. The compositional zones defined here provide a compositional and structural foundation on which to base further analyses. This overview of the SPA interior and surroundings can also guide preparation for the return of samples from the SPA, as repeatedly and strongly recommended by the National Research Council (2003, 2011).

Acknowledgments
We greatly appreciate support for this work through the NASA LASER (NNX12AI96G) and SSERVI (NNA14AB01A) programs. The authors thank James W. Head for invaluable discussion while developing the manuscript. Reviews from David Trang and an anonymous reviewer were immensely helpful in sharpening, clarifying, and improving the paper. The Level 2 M^3 data used in this analysis are available through the Planetary Data System Imaging Node (https://pds-imaging.jpl.nasa.gov/volumes/m3.html). Spectra shown throughout the manuscript were obtained from the M^3 files specified in Table S1. The Lunar Reconnaissance Orbiter Wide Angle Camera mosaics used here are available from the LROC team (http://wms.lroc.asu.edu/lroc/view_rdr/WAC_GLOBAL). The Lunar Orbiter Laser Altimeter topography used here are available through the Planetary Data System Geosciences Node (http://pds-geosciences.wustl.edu/missions/lro/lola.htm). The Lunar Prospector Iron Abundance maps and Geologic Maps (used to mask mare basalts) are available through the USGS PIGWAD server (https://webgis.wr.usgs.gov/pigwad/maps/the_moon.htm). Filenames for the RELAB spectra shown in Figure are given in the caption, and the spectra are available online (http://www.planetary.brown.edu/relabdocs/relab.htm). Data and spectra for Lunar Rock and Mineral Characterization Consortium and Lunar Soil Characterization Consortium samples are available through RELAB (http://www.planetary.brown.edu/relabdocs/relab_related_data.htm).

References

Besse, S., Sunshine, J., Staid, M., Boardman, J., Pieters, C., Guasqui, P., et al. (2013). A visible and near-infrared photometric correction for Moon Mineralogy Mapper (M 3). *Icarus*, *222*(1), 229–242. https://doi.org/10.1016/j.icarus.2012.10.036

Blewett, D. T., Taylor, G. J., Lucey, P. G., Hawke, B. R., & Gillis, J. (1999). High-resolution, quantitative remote sensing of South Pole-Aitken Basin. In *Lunar and Planetary Science Conference* (Vol. 30, p. 1438).

Boardman, J. W., Pieters, C. M., Green, R. O., Lundeen, S. R., Varanasi, P., Nettles, J., et al. (2011). Measuring moonlight: An overview of the spatial properties, lunar coverage, selenolocation, and related Level 1B products of the Moon Mineralogy Mapper. *Journal of Geophysical Research*, *116*, E00G14. https://doi.org/10.1029/2010JE003730

Burns, R. G. (1993). *Mineralogical Applications of Crystal Field Theory* (2nd ed. p. 551). Cambridge, UK: Cambridge University Press. https://doi.org/10.1017/CBO9780511524899

Cahill, J. T. S., Lucey, P. G., & Wieczorek, M. A. (2009). Compositional variations of the lunar crust: Results from radiatative transfer modeling of central peak spectra. *Journal of Geophysical Research*, *114*, E09001. https://doi.org/10.1029/2008JE003282

Cassanelli, J. P., & Head, J. W. III (2016). Did the Orientale impact melt sheet undergo large-scale igneous differentiation by crystal settling? *Geophysical Research Letters*, *43*, 11,156–11,165. https://doi.org/10.1002/2016GL070425

Cheek, L. C., et al. (2011). Spectral characteristics of plagioclase with variable iron content: Applications to remote sensing of the lunar crust. *Lunar and Planetary Science*, *42*, 1617.

Cintala, M. J., & Grieve, R. A. F. (1994). The effects of differential scaling of impact melt and crater dimensions on lunar and terrestrial craters: Some brief examples. In *Large meteorite impacts and planetary evolution, Geological Society of America Special Paper* (Vol. 293, p. 51). Boulder, CO.

Cintala, M. J., & Grieve, R. A. F. (1998). Scaling impact melting and crater dimensions: Implications for the lunar cratering record. *Meteoritics and Planetary Science*, *33*(4), 889–912. https://doi.org/10.1111/j.1945-5100.1998.tb01695.x

Cloutis, E. A., & Gaffey, M. J. (1991). Pyroxene spectroscopy revisited: Spectral-compositional correlations and relationship to geothermometry. *Journal of Geophysical Research*, *96*, 22,809–22,826.

Elkins-Tanton, L. T., & Hager, B. H. (2005). Giant meteoroid impacts can cause volcanism. *Earth and Planetary Science Letters*, *239*, 219–232.

Garrick-Bethell, I., & Zuber, M. T. (2009). Elliptical structure of the lunar South Pole-Aitken Basin. *Icarus*, *204*(2), 399–408. https://doi.org/10.1016/j.icarus.2009.05.032

Goswami, J. N., & Annadurai, M. (2009). Chandrayaan-1: India's first planetary science mission to the Moon. *Current Science*, *96*, 486–491.

Green, R. O., Pieters, C., Mouroulis, P., Eastwood, M., Boardman, J., Glavich, T., et al. (2011). The Moon Mineralogy Mapper (M^3) imaging spectrometer for lunar science: Instrument description, calibration, on-orbit measurements, science data calibration and on-orbit validation. *Journal of Geophysical Research*, *116*, E00G19. https://doi.org/10.1029/2011JE003797

Hammond, N. P., Nimmo, F., & Korykansky, D. (2009). Hydrocode modeling of the South Pole Aitken Basin-forming impact. In *40th Lunar and Planetary Science Conference*, Abstract 1455.

Head, J. W., Fassett, C. I., Kadish, S. J., Smith, D. E., Zuber, M. T., Neumann, G. A., & Mazarico, E. (2010). Global distribution of large lunar craters: Implications for resurfacing and impactor populations. *Science*, *329*, 1504–1507. https://doi.org/10.1126/science.1195050

Hurwitz, D. M., & Kring, D. A. (2014). Differentiation of the South Pole-Aitken Basin impact melt sheet: Implications for lunar exploration. *Journal of Geophysical Research: Planets*, *119*, 1110–1113. https://doi.org/10.1002/2013JE004530

Isaacson, P. J., Sarbadhikari, A. B., Pieters, C. M., Klima, R. L., Hiroi, T., Liu, Y., & Taylor, L. A. (2011). The lunar rock and mineral characterization consortium: Deconstruction and integrated mineralogical, petrologic, and spectroscopic analyses of mare basalts. *Meteoritics & Planetary Science*, *46*(2), 228–251. https://doi.org/10.1111/j.1945-5100.2010.01148.x

Isaacson, P. J., Petro, N. E., Pieters, C. M., Besse, S., Boardman, J. W., Clark, R. N., et al. (2013). Development, importance, and effect of a ground truth correction for the Moon Mineralogy Mapper reflectance data set. *Journal of Geophysical Research: Planets*, *118*, 369–381. https://doi.org/10.1002/jgre.20048

Jolliff, B. L., Gillis, J. J., Haskin, L. A., Korotev, R. L., & Wieczorek, M. A. (2000). Major lunar crustal terranes: Surface expressions and crust-mantle origins. *Journal of Geophysical Research*, *105*(E2), 4197–4216. https://doi.org/10.1029/1999JE001103

Jolliff, B. L., Haskin, L. A., Korotev, R. L., Papike, J. J., Shearer, C. K., Pieters, C. M., & Cohen, B. A. (2003). Scientific expectations from a sample of regolith and rock fragments from the interior of the lunar South Pole-Aitken Basin. In *34th Annual Lunar and Planetary Science Conference*, Abstract 1989.

Jolliff, B. L., Alkalai, L., Pieters, C. M., Head, J. W., Papanastassiou, D. A., & Bierhaus, E. B. (2010). Sampling the South Pole-Aitken Basin: Objectives and site selection criteria. In *41st Lunar and Planetary Science Conference*, Abstract 2450.

Jolliff, B. L., Shearer, C. K., Papanastassiou, D. A., & Liu, Y. (2017). Why do we need samples from the Moon's South Pole-Aitken Basin and what would we do with them? In *48th Lunar and Planetary Science Conference*, Abstract 1300.

Kadish, S. J., Fassett, C. I., Head, J. W., Smith, D. E., Zuber, M. T., Neumann, G. A., & Mazarico, E. (2011). A global catalog of large lunar crater (≥20 KM) from the Lunar Orbiter Laser Altimeter. In *42nd Lunar and Planetary Science Conference*, Abstract 1006.

Klima, R. L., Pieters, C. M., & Dyar, M. D. (2007). Spectroscopy of synthetic Mg-Fe pyroxenes I: Spin-allowed and spin-forbidden crystal field bands in the visible and near-infrared. *Meteoritics and Planetary Science*, *42*(2), 235–253. https://doi.org/10.1111/j.1945-5100.2007.tb00230.x

Klima, R. L., Dyar, M. D., & Pieters, C. M. (2011). Near-infrared spectra of clinopyroxenes: Effects of calcium content and crystal structure. *Meteoritics and Planetary Science*, *46*(3), 379–395. https://doi.org/10.1111/j.1945-5100.2010.01158.x

Klima, R. L., Pieters, C. M., Boardman, J. W., Green, R. O., Head, J. W. III, Isaacson, P. J., et al. (2011). Insights into lunar petrology: Distribution and composition of prominent low-Ca pyroxene exposures as observed by Moon Mineralogy Mapper (M^3). *Journal of Geophysical Research*, *116*, E00G06. https://doi.org/10.1029/2010JE003719

Kramer, G. Y., Kring, D. A., Nahm, A. L., & Pieters, C. M. (2013). Spectral and photogeologic mapping of Schrödinger Basin and implications for post-South Pole-Aitken impact deep subsurface stratigraphy. *Icarus*, *223*(1), 131–148. https://doi.org/10.1016/j.icarus.2012.11.008

Kring, D. A., McGovern, P. J., Potter, R. W. K., Collins, G. S., Grange, M. L., & Nemchin, A. A. (2015). Was an epoch of lunar magmatism triggered by the South Pole - Aitken Basin Impact? *Early Solar System Impact Bombardment III*, Abstract 3009.

Lawrence, D. J., Feldman, W. C., Elphic, R. C., Little, R. C., Prettyman, T. H., Maurice, S., et al. (2002). Iron abundances on the lunar surface as measured by the Lunar Prospector gamma-ray and neutron spectrometers. *Journal of Geophysical Research*, *107*(E12), 5130. https://doi.org/10.1029/2001JE001530

Lucey, P. G., Taylor, G. J., Hawke, B. R., & Spudis, P. D. (1998). FeO and TiO2 concentrations in the South Pole-Aitken Basin: Implications for mantle composition and basin formation. *Journal of Geophysical Research*, *103*(E2), 3701–3708. https://doi.org/10.1029/97JE03146

Lundeen, S., McLaughlin, S., & Alanis, R. (2011). Moon mineralogy mapper data product software interface specification. PDS document version 9.10, jet Propulsion Laboratory, JPL D-39032, Pasadena, CA.

Melosh, H. J. (1989). *Impact Cratering: A Geologic Process*. New York, NY: Oxford University Press.

Moriarty, D. P. III, & Pieters, C. M. (2015). The nature and origin of mafic mound in the South Pole-Aitken Basin. *Geophysical Research Letters*, *42*, 7907–7915. https://doi.org/10.1002/2015GL065718

Moriarty, D. P. III, & Pieters, C. M. (2016a). Complexities in pyroxene compositions derived from absorption band centers: Examples from Apollo samples, HED meteorites, synthetic pure pyroxenes, and remote sensing data. *Meteoritics and Planetary Science*, *51*(2), 207–234. https://doi.org/10.1111/maps.12588

Moriarty, D. P. III, & Pieters, C. M. (2016b). Impact melt and magmatic processes in central South Pole-Aitken Basin. In *47th Lunar and Planetary Science Conference*, Abstract 1735.

Moriarty, D. P. III, & Pieters, C. M. (2016c). South Pole-Aiken Basin as a probe to the lunar interior. In *47th Lunar and Planetary Science Conference*, Abstract 1763.

Moriarty, D. P., Pieters, C. M., & Isaacson, P. J. (2013). Compositional heterogeneity of central peaks within the South Pole-Aitken Basin. *Journal of Geophysical Research: Planets*, *118*, 2310–2322. https://doi.org/10.1002/2013JE004376

Morrison, D. A. (1998). Did a thick South Pole-Aitken Basin melt sheet differentiate to form cumulates? In *29th Lunar and Planetary Science Conference*, Abstract 1657.

Nakamura, R., Matsunaga, T., Ogawa, Y., Yamamoto, S., Hiroi, T., Saiki, K., et al. (2009). Ultramafic impact melt sheet beneath the South Pole-Aitken Basin on the Moon. *Geophysical Research Letters*, *36*, L22202. https://doi.org/10.1029/2009GL040765

National Research Council (2003). *New Frontiers in the Solar System: An Integrated Exploration Strategy*. Washington, DC: National Academies Press.

National Research Council (2011). *Vision and Voyages for Planetary Science in the Decade 2013–2022*. Washington, DC: National Academies Press.

Nelson, D. M., Koeber, S. D., Daud, K., Robinson, M. S., Watters, T. R., Banks, M. E., & Williams, N. R. (2014). Mapping lunar maria extents and lobate scarps using LROC image products. In *45th Lunar and Planetary Science Conference*, Abstract 2861.

Noble, S. K., Pieters, C. M., Hiroi, T., & Taylor, L. A. (2006). Using the modified Gaussian model to extract quantitative data from lunar soils. *Journal of Geophysical Research*, *111*, E11009. https://doi.org/10.1029/2006JE002721

Ohtake, M., Uemoto, K., Yokota, Y., Morota, T., Yamamoto, S., Nakamura, R., et al. (2014). Geologic structure generated by large-impact basin formation observed at the South Pole-Aitken Basin on the Moon. *Geophysical Research Letters*, *41*, 2738–2745. https://doi.org/10.1002/2014GL059478

Petro, N. E., Mest, S. C., & Teich, Y. (2011). Geomorphic terrains and evidence for ancient volcanism within northeastern South Pole-Aitken Basin. *Geological Society of America Special Papers*, *477*, 129–140.

Pieters, C. M. (2017). *Origin and Importance of 'Featureless' Plagioclase on the Moon*. Münster, Germany: European Lunar Symposium.

Pieters, C. M., & Taylor, L. A. (2003). Systematic mixing and melting in lunar soil evolution. *Geophysical Research Letters*, *30*(20), 2048. https://doi.org/10.1029/2003GL018212

Pieters, C. M., Taylor, L. A., Noble, S. K., Keller, L. P., Hapke, B., Morris, R. V., et al. (2000). Space weathering on airless bodies: Resolving a mystery with lunar samples. *Meteoritics & Planetary Science*, *35*(5), 1101–1107. https://doi.org/10.1111/j.1945-5100.2000.tb01496.x

Pieters, C. M., Head, J. W., Gaddis, L., Jolliff, B., & Duke, M. (2001). Rock types of South Pole-Aitken Basin and extent of basaltic volcanism. *Journal of Geophysical Research*, *106*(E11), 28,001–28,022. https://doi.org/10.1029/2000JE001414

Pieters, C. M., Boardman, J., Buratti, B., Chatterjee, A., Clark, R., Glavich, T., et al. (2009). The Moon Mineralogy Mapper (M^3) on Chandrayaan-1. *Current Science*, *96*(4), 500–505.

Potter, R. W. K., Collins, G. S., Kiefer, W. S., McGovern, P. J., & Kring, D. A. (2012). Constraining the size of the South Pole-Aitken Basin impact. *Icarus*, *220*(2), 730–743. https://doi.org/10.1016/j.icarus.2012.05.032

Robinson, M. S., Brylow, S. M., Tschimmel, M., Humm, D., Lawrence, S. J., Thomas, P. C., et al. (2010). Lunar Reconnaissance Orbiter Camera (LROC) instrument overview. *Space Science Reviews*, *150*(1-4), 81–124. https://doi.org/10.1007/s11214-010-9634-2

Scott, D. H., & McCauley, J. F. (1977). *Geologic map of the west side of the Moon*. Reston, VA: U.S. Geological Survey.

Schultz, P. H., & Crawford, D. A. (2011). Origin of nearside structural and geochemical anomalies on the Moon. *Geological Society of America Special Papers*, *477*, 141–159. https://doi.org/10.1130/2011.2477(07)

Smith, D. E., Zuber, M. T., Neumann, G. A., Lemoine, F. G., Mazarico, E., Torrence, M. H., & Aharonson, O. (2010). Initial observations from the Lunar Orbiter Laser Altimeter (LOLA). *Geophysical Research Letters*, *37*, L18204. https://doi.org/10.1029/2010GL043751

Spudis, P. D., Reisse, R. A., & Gillis, J. J. (1994). Ancient multiring basins on the Moon revealed by Clementine laser altimetry. *Science*, *266*(5192), 1848–1851. https://doi.org/10.1126/science.266.5192.1848

Stewart, S. T. (2011). Impact basin formation: The mantle excavation paradox resolved. In *42nd Lunar and Planetary Science Conference*, Abstract1633

Stuart-Alexander, D. E. (1978). *Geologic Map of the Central Far Side of the Moon*. Reston, VA: U.S. Geological Survey.

Sunshine, J. M., Pieters, C. M., & Pratt, S. F. (1990). Deconvolution of mineral absorption bands: An improved approach. *Journal of Geophysical Research*, *95*(B5), 6955–6966. https://doi.org/10.1029/JB095iB05p06955

Taylor, L. A., Pieters, C. M., Keller, L. P., Morris, R. V., & McKay, D. S. (2001). Lunar mare soils: Space weathering and the major effects of surface-correlated nanophase Fe. *Journal of Geophysical Research*, *106*(E11), 27,985–27,999. https://doi.org/10.1029/2000JE001402

Taylor, L. A., Pieters, C. M., Patchen, A., Taylor, D. S., Morris, R. V., Keller, L. P., & McKay, D. S. (2010). Mineralogical and chemical characterization of lunar highland soils: Insights into the space weathering of soils on airless bodies. *Journal of Geophysical Research*, *115*, E02002. https://doi.org/10.1029/2009JE003427

Tompkins, S., & Pieters, C. M. (1999). Mineralogy of the lunar crust: Results from Clementine. *Meteoritics and Planetary Science*, *34*(1), 25–41. https://doi.org/10.1111/j.1945-5100.1999.tb01729.x

Vaughan, W. M., & Head, J. W. III (2014). Impact melt differentiation in the South Pole-Aitken Basin: Some observations and speculations. *Planetary and Space Science*, *91*, 101–106. https://doi.org/10.1016/j.pss.2013.11.010

Vaughan, W. M., Head, J. W., Wilson, L., & Hess, P. C. (2013). Geology and petrology of enormous volumes of impact melt on the Moon: A case study of the Orientale basin impact melt sea. *Icarus*, *223*(2), 749–765. https://doi.org/10.1016/j.icarus.2013.01.017

Warren, P. H., Claeys, P., & Cedillo-Pardo, E. (1996). Mega-impact melt petrology (Chicxulub, Sudbury, and the Moon): Effects of scale and other factors on potential for fractional crystallization and development of cumulates. The Cretaceous-Tertiary event and other catastrophes in Earth history, 105–124.

Whitten, J. L., & Head, J. W. III (2014). Lunar cryptomaria: Physical characteristics, distribution, and implications for ancient volcanism. *Icarus*, *247*, 150–171.

Wilhelms, D. E., & El-Baz, F. (1977). *Geological Map of the East Side of the Moon*. Reston, VA: U.S. Geological Survey.

Wilhelms, D. E., Howard, K. A., & Wilshire, H. G. (1979). *Geologic map of the south side of the Moon*. Reston, VA: U.S. Geological Survey.

Wilhelms, D. E., McCauley, J. F., & Trask, N. J. (1987). *The Geologic History of the Moon, USGS Professional Paper, 1348* (p. 302).

Yamamoto, S., Nakamura, R., Matsunaga, T., Ogawa, Y., Ishihara, Y., Morota, T., et al. (2012). Olivine-rich exposures in the South Pole-Aitken Basin. *Icarus*, *218*(1), 331–344. https://doi.org/10.1016/j.icarus.2011.12.012

Yingst, R. A., & Head, J. W. III (1999). Geology of the mare deposits in South Pole-Aitken Basin as seen by Clementine UVVIS data. *Journal of Geophysical Research*, *104*(E8), 18,957–18,979. https://doi.org/10.1029/1999JE900016